Journal of Materials Chemistry A

ROYAL SOCIETY OF CHEMISTRY

PAPER

View Article Online
View Journal | View Issue

Cite this: J. Mater. Chem. A, 2025, 13, 33671

Ion-selective transport in surface-modified cellulose membranes for aqueous ionic thermoelectrics

Anjali Ashokan, [abc] Kamil Rahme,[ab] Rupa Ranjani Palanisamy,[ac] N. Padmanathan,[c] Kafil M. Razeeb, [c] Subhajit Biswas *[ab] and Justin D. Holmes *[ab]

Efficient recovery of low-grade heat (≤100 °C) remains a significant challenge in sustainable energy conversion. Here, we report a strategy to enhance ionic thermoelectric performance in biocompatible regenerated cellulose (RC) membranes by tailoring their surface charge. Surface functionalisation was achieved using two oppositely charged organic moieties: 2,2,6,6-tetramethylpiperidin-1-oxyl (TEMPO) to introduce carboxyl groups, and 3-chloro-2-hydroxypropyltrimethylammonium chloride (CHMAC) to graft quaternary ammonium functionalities. This work presents the first direct, side-by-side comparison of oppositely charged surface functional groups, carboxyl (TEMPO) and quaternary ammonium (CHMAC), on ionic thermoelectric behaviour in cellulose membranes. These modifications significantly increased the fixed surface charge density, promoting ion selectivity and enabling efficient ion transport under a thermal gradient. CHMAC-functionalised RC membranes exhibited the highest performance, with a Seebeck coefficient of +6.1 mV K^{-1} in a stacked membrane configuration using 0.1 mM HCl electrolyte, representing a tenfold enhancement compared to unmodified RC membranes. Correspondingly, ionic conductivity increased by up to 950-fold, with an ionic thermoelectric power factor of 1.38 μW m^{-1} K^{-2}. This study establishes a clear link between surface charge engineering and thermodiffusion-enhanced ionic transport in RC membranes, offering a scalable and sustainable route for harvesting low-grade thermal energy using green, aqueous systems.

Received 30th June 2025
Accepted 1st September 2025

DOI: 10.1039/d5ta05281e

rsc.li/materials-a

Introduction

Nanofluidic membranes, originally developed for filtration and separation, are now being increasingly applied in ion regulation across various fields, including renewable energy, industrial processing, and biomedical applications.[1–3] Electrokinetic transport through these membranes has gained considerable interest due to its relevance in energy conversion systems, including osmotic power generation,[4,5] thermoelectrics,[6] molecular and ionic separation,[7] and advanced liquid separation techniques such as nanofiltration.[8] A defining property of nanofluidic membranes is their uncharacteristic high ionic conductance in low-concentration electrolytes, deviating from classic bulk behaviour.[9,10] This phenomenon arises from surface charge effects: interactions between polarisable electrolytes and charged nanopore walls result in the formation of an electrical double layer enriched in counter-ions and depleted in co-ions.[11] Consequently, selective ion migration, predominantly of counter-ions, enhances ionic conductivity beyond that of the bulk solution. However, this surface-governed conductance is diminished when the electrolyte concentration exceeds the fixed surface charge, giving way to bulk-dominated transport.[12] Typically, surface charge-driven ion transport is observed at electrolyte concentrations below 10 mM, transitioning to bulk behaviour at higher concentrations.[12–14] Recently, such ion-selective nanofluidic membranes have shown promise in ionic thermoelectric applications, where a temperature gradient across the membrane drives directional ion movement and generates a thermoelectric voltage.[15–17] This approach is particularly attractive for converting low-grade waste heat, which is ubiquitous yet underutilised, into usable electrical energy, thereby addressing both energy efficiency and sustainability goals.[18–20] However, conventional solid-state thermoelectric generators rely on scarce and often toxic materials, limiting their scalability and environmental compatibility. In contrast, ionic thermoelectric devices based on sustainable membranes offer a green and potentially scalable alternative for converting thermal energy to electricity.[21–23]

Precise control of surface charge in nanofluidic membranes is a key strategy for enhancing ion transport and boosting the performance of ionic thermoelectric (i-TE) systems. This can be

[a]School of Chemistry, University College Cork, Cork, T12 YN60, Ireland. E-mail: s.biswas@ucc.ie; j.holmes@ucc.ie

[b]AMBER Centre, Environmental Research Institute, University College Cork, Cork, T23 XE10, Ireland

[c]Micro-Nano System Centre, Tyndall National Institute, Cork, T12 R5CP, Ireland

achieved through chemical functionalisation with charged organic groups, which significantly increases the fixed surface charge density.[24] An increased surface charge promotes ion selectivity by facilitating the enrichment of counter-ions and the exclusion of co-ions, thereby enhancing ionic conductivity. Additionally, the geometry of membrane nanochannels also plays a crucial role.[9] In confined channels infiltrated with electrolyte, the surface charge induces the formation of an electrical double layer (EDL), where electrostatic interactions dominate over bulk diffusion. These EDL effects are amplified in narrow pores, promoting the selective transport of counter-ions while suppressing co-ion mobility. These EDLs favour directional counter-ion migration while suppressing co-ion mobility, leading to enhanced ion separation under thermal gradients. This selective ion transport is key to achieving high Seebeck coefficients and thermovoltage output in i-TE devices. Accordingly, both the surface charge density and the nanostructure of the membrane are critical to the design of efficient i-TE materials.[25]

Nanofluidic membranes can be categorised into one-, two-, and three-dimensional (1D, 2D, and 3D) architectures based on their ionic transport pathways. Among these, 3D nanofluidic membranes, with their interconnected porous networks, offer increased surface area and enhanced fluid–material interactions, enabling efficient ion regulation. Their structural tunability, across pore size, shape, and morphology, makes them attractive platforms, particularly when fabricated from flexible polymeric materials.[26,27] However, widespread use of synthetic polymers is constrained by environmental and sustainability concerns. In this context, cellulose has emerged as a promising alternative. As a renewable, biodegradable, and biocompatible polymer, cellulose supports the development of eco-friendly nanofluidic devices. Cellulose-based membranes are already well-established in separation technologies and flexible electronics[28–31] and are now gaining traction in i-TE applications.[16] When infiltrated with electrolytes and subject to a thermal gradient, RC membranes exhibit electroosmotic flow, enabling directional ion migration.[6] By tailoring their surface charge through functionalisation, both ionic conductivity and ion selectivity can be significantly improved, enhancing charge separation at the electrodes and resulting in higher thermovoltage output.[32] Additionally, the intrinsically low thermal conductivity of cellulose helps maintain thermal gradient, further benefiting i-TE performance. Notably, cellulose's abundance of hydroxyl groups enables versatile surface modification. For example, TEMPO-mediated oxidation, which converts hydroxyl to carboxyl groups, has been shown to increase surface charge density by 1.5-fold and deliver thermovoltage outputs as high as 24 mV K^{-1}.[16] Similarly, Jia *et al.*[33] reported highly charged bacterial cellulose/boron nitride composites achieving excellent ion selectivity and energy conversion under low-grade thermal gradients. Their system demonstrated a power density of 10 W m^{-2} using river and seawater, illustrating the potential of cellulose-based nanofluidics for simultaneous thermal and osmotic energy harvesting. These advances underscore the promise of functionalised cellulose as a sustainable material for next-generation i-TE devices.

In this study, we report a surface-charge engineering strategy for regenerated cellulose (RC) membranes that enables exceptional enhancement of ionic conductivity and i-TE response under aqueous conditions. Commercial RC membranes with varying pore sizes were functionalised with negatively charged carboxyl groups *via* 2,2,6,6-tetramethylpiperidin-1-yl)oxy (TEMPO) oxidation and positively charged quaternary ammonium groups *via* 3-chloro-2-hydroxypropyl)trimethylammonium chloride (CHMAC) etherification. While the absolute values of ionic conductivity and Seebeck coefficients are comparable to those in earlier studies, the novelty of this work lies in the magnitude of enhancement achieved through controlled surface functionalisation, resulting in a 950-fold increase in ionic conductivity and a tenfold boost in thermovoltage output compared to unmodified RC membranes. This dual-functionalisation approach provides a rare side-by-side comparison of surface charge polarity effects on i-TE behaviour. Detailed characterisation *via* Fourier-transform infrared (FT-IR) spectroscopy, scanning electron microscopy (SEM), contact angle measurements, zeta potential analysis, and X-ray photoelectron spectroscopy (XPS) confirmed the successful functionalisation. At the same time, electrochemical impedance spectroscopy (EIS) and linear sweep voltammetry (LSV) were used to correlate conductivity with surface charge density. Thermoelectric performance was evaluated in both in-plane and cross-plane configurations using low-concentration HCl electrolyte, demonstrating robust, surface-charge-governed i-TE behaviour. This work presents a sustainable and scalable platform for tailoring ionic transport in biopolymer membranes, highlighting the critical role of surface charge density in amplifying i-TE effects, even under low ionic strength conditions.

Experimental

Materials

Regenerated cellulose (RC) membrane discs with nominal pore sizes of 0.2 μm (RC-200, 47 mm disc diameter), 0.45 μm, (RC-450, 50 mm disc diameter), and 1 μm (RC-1k, 47 mm disc diameter) were obtained from Sigma-Aldrich. The nominal pore sizes were specified by the manufacturer based on standard characterisation techniques, including bubble point testing and liquid (water) flow rate and retention measurements. All reagents were used as received without further purification, including sodium hydroxide (NaOH), sodium sulfite (Na_2SO_3), hydrogen peroxide (H_2O_2, 35 wt%), 2,2,6,6-tetramethylpiperidine 1-oxyl (TEMPO, $C_9H_{18}NO$), sodium bromide (NaBr), sodium hypochlorite (NaClO, 6–14% active chlorine), 3-chloro-2-hydroxypropyl)trimethylammonium chloride (CHMAC, 60 wt% solution), and SYLGARD™ 184 silicone elastomer kit. All chemicals were purchased from Sigma-Aldrich unless otherwise stated.

Synthesis of TEMPO functionalised RC membranes

TEMPO-mediated oxidation was employed to introduce carboxyl groups onto RC membranes by converting surface

hydroxyl groups.[34] 1 g of RC membrane was immersed in 100 mL of deionised water and equilibrated. TEMPO (0.016 g) and NaBr (0.1 g) were then added to the suspension. The pH of the solution was adjusted to 10–10.3 using 0.5 M NaOH, followed by the introduction of NaClO (5 mmol) to initiate oxidation. The pH was maintained within this range for 2.5 h by dropwise addition of 0.5 M NaOH or 1 M HCl as needed. The reaction was then quenched by adjusting the pH to 7 with HCl. Functionalised membranes were thoroughly rinsed with 1 M HCl to remove residual reagents, then subjected to sequential solvent exchange with acetone and toluene. The functionalised membranes were air-dried before characterisation.

Synthesis of CHMAC functionalised RC membranes

Quaternary ammonium groups were introduced onto RC membranes *via* CHMAC functionalisation.[35] RC membranes (0.4 wt%) were dispersed in a 2 wt% NaOH solution and allowed to equilibrate. CHMAC (5 wt%) was then added dropwise to the solution under continuous mechanical stirring. The reaction mixture was maintained at 65 °C for 16 h to ensure complete functionalisation. After the reaction, membranes were thoroughly washed with deionised water to remove unreacted CHMAC and residual by-products. The functionalised membranes were air-dried and stored for subsequent characterisation.

Structural and surface characterisation

The chemical composition and surface functionalisation of pure RC, TEMPO-functionalised RC (TEMPO-RC) and CHMAC-functionalised RC (CHMAC-RC) membranes were characterised using multiple analytical techniques. Fourier-transform infrared (FT-IR) spectroscopy was performed using a PerkinElmer spectrometer on 2 × 2 cm^2 membrane samples to identify characteristic functional groups. Surface wettability was evaluated using static water contact angle measurements with an Ossila contact angle goniometer, employing the same membrane dimensions. To quantify the extent of CHMAC functionalisation, X-ray photoelectron spectroscopy (XPS) was conducted on the membrane surfaces before and after modification. XPS spectra were acquired using a Kratos Axis Ultra instrument equipped with a monochromatic Al K_α source (1486.58 eV). Survey spectra were collected with a pass energy of 160 eV and a step size of 1 eV, while high-resolution spectra were recorded using a pass energy of 20 eV and a step size of 0.05 eV.

For surface morphology analysis, membrane samples (approximately 0.3 × 0.3 cm^2) were examined using a Quanta 650 scanning electron microscope (SEM). To evaluate the surface charge characteristics, both pristine and functionalised RC membranes were dispersed in water at a concentration of 0.01 wt% and stirred vigorously overnight to ensure uniform suspension. Zeta potential measurements were then performed on the resulting dispersions using a Zetasizer Nano S90 (Malvern Instruments).

The concentration of negatively charged functional groups on pristine and TEMPO-functionalised RC membranes was quantified *via* conductometric titration. Membrane samples (40 mg) were dispersed in 40 mL of deionised water under continuous stirring to ensure complete dispersion. To protonate carboxyl groups, 15 μL of 1 M HCl was added, followed by 60 μL of 1 M NaCl to stabilise ionic strength. The resulting solution was titrated with 0.01 M NaOH, while monitoring conductivity using an Orion Versa Star Pro conductivity meter (Thermo Fisher Scientific). The surface charge density (σ) was calculated using eqn (1).[16]

$$\sigma = \frac{C(V_2 - V_1)}{m} \quad (1)$$

where, C is the concentration of the NaOH titrant (mol L^{-1}), m is the mass of the membrane sample (g), and V_1 and V_2 are the volumes of titrant (mL) required to neutralise the added strong acid and the membrane-bound weak acidic groups, respectively.

Ionic conductivity measurements

Pristine and functionalised RC membranes were cut into rectangular strips and embedded in SYLGARD™ 184 silicone elastomer. After curing, two reservoirs were created to expose both ends of the membrane to the electrolyte. The assembled nanofluidic devices were hydrated in Milli-Q water (resistance: 18 MΩ) for 48 h. Before measurements, the devices were immersed in electrolyte for at least 24 h to ensure thorough membrane wetting. The choice of 10^{-4} M HCl as the electrolyte reflects a strategic focus on low ionic strength conditions, which not only favour surface-governed conduction but also mimic environments relevant to sustainable sensing and biocompatible devices. Although dilute aqueous HCl (10^{-5}–10^{-2} M) was used to precisely control pH and ionic strength during characterisation, the extremely low concentrations and volumes pose minimal environmental risk. The overall system remains sustainable due to the use of renewable cellulose, water-based processing, and negligible electrolyte usage. Silver/silver chloride (Ag/AgCl) electrodes were prepared by soaking Ag wires in NaOCl solution for 48 h, followed by rinsing with deionised water. Ionic conductivity was evaluated using both linear sweep voltammetry (LSV) and electrochemical impedance spectroscopy (EIS). LSV measurements were performed using a Biologic SP-50e potentiostat at a scan rate of 10 mV s^{-1} over a voltage window of ±0.4 V. EIS was conducted by applying a 10 mV AC voltage across a frequency range of 1 MHz to 65 Hz. Ionic conductivity (κ, S m^{-1}) values were calculated using eqn (2):

$$\kappa = \frac{GL}{wh} \quad (2)$$

where G is the measured conductance (S), L is the distance between electrodes (m), w is the membrane width (m), and h is the membrane thickness (m).[35,36]

Thermoelectric characterisation

The in-plane thermoelectric properties of pristine and functionalised RC membranes were measured using a custom-built setup (Fig. S1, SI). Membranes were cut into rectangular strips

and soaked in 10^{-4} M HCl overnight to ensure complete electrolyte infiltration. Each membrane was then mounted onto a gold-coated silicon wafer using thermal paste and fixed to a Peltier element connected to a programmable power supply. This allowed precise control of the temperature gradient across the membrane. Gold electrodes were used to collect the thermoelectric output, and the resulting open-circuit voltage was recorded using a voltmeter.

To evaluate cross-plane (perpendicular) thermoelectric performance, a stacked membrane configuration was employed using a modified ASTM D5470-06-based setup (Fig. S2, SI).[37] Membranes were cut into 1×1 cm^2 squares, infiltrated with 10^{-4} M HCl overnight, and stacked between two gold-coated silicon wafer electrodes. The sandwich assembly was placed between two copper rods, with one end connected to a Peltier cooler and the other to a heat source, both of which were controlled *via* an external power supply. The open-circuit voltage generated under the applied thermal gradient was recorded using an electrochemical workstation. Temperature differences across the cell were accurately measured using four thermistors, each positioned on a separate copper rod to monitor local temperatures.

Results and discussion

The pore size and surface charge density of RC membranes are key parameters governing their ionic conductivity and thermoelectric behaviour, particularly at lower electrolyte concentrations. To investigate these effects, three variants of flexible, paper-like RC membranes with nominal pore sizes of 1 μm (RC-1k), 450 nm (RC-450), and 200 nm (RC-200) were selected. Each membrane type was subjected (see Experimental section) to a detailed functionalisation process with oppositely charged moieties: negatively charged carboxyl groups *via* TEMPO oxidation and positively charged quaternary ammonium groups *via* CHMAC etherification. The resulting functionalised, electrolyte-infiltrated RC membranes were characterised to assess their morphological, surface, electrochemical, and thermoelectric properties.

Surface morphology analysis using SEM (Fig. 1) revealed that all RC membranes exhibit a fibrous, interconnected porous network formed by overlapping cellulose microfibrils. This fibrous structure extends continuously across the membrane surface and throughout its thickness. Notably, the fibrous morphology also suggests that the nominal pore size may not reflect the actual ionic transport environment. The overlapping microfibrils can form highly tortuous and distorted pathways, creating regions of confinement and enhanced surface interaction. These quasi-nanoconfined domains can effectively amplify the impact of surface charge, even in membranes with micrometre-scale nominal pores. Cross-sectional SEM images (Fig. S3, SI) showed that the RC-200 and RC-1k membranes have comparable thicknesses of approximately 40 μm, whereas RC-450 exhibits a slightly greater thickness of around 70 μm. These morphological features support ion-permeable porosity and provide a robust matrix for surface functionalisation and ion transport.

Functionalisation of RC membranes

The fibrous morphology of the RC membranes was retained following surface functionalisation, as confirmed by SEM imaging (Fig. S4, SI). Cellulose naturally contains a high abundance of hydroxyl groups, which act as the primary sites for chemical functionalisation and contribute to a slight negative surface charge. Zeta potential measurements of the pristine RC membranes in 0.01 wt% aqueous dispersion (pH of 6.5) gave values of -17.4 ± 0.4 mV for RC-200, -19.6 ± 4.4 mV for RC-450, and -11.7 ± 2.4 mV for RC-1k, reflecting differences in pore structure, fibre morphology, and effective surface area, despite having the same underlying surface chemistry. To enhance the negative surface charge, TEMPO-mediated oxidation was employed to convert hydroxyl groups to carboxyl groups *via* a well-established radical oxidation pathway involving TEMPO, NaBr, and NaClO as catalysts (Scheme S1(a), in SI).[34] This modification significantly increased the zeta potential magnitude, yielding -28.9 ± 3.4 mV for TEMPO-RC-200, -30.67 ± 0.95 mV for TEMPO-RC-450, and -21.8 ± 0.4 mV for TEMPO-RC-1k (0.01 wt% solution, pH ~5). The greater negative charge arises from the dissociation of carboxyl groups into carboxylate ions, which occurs more readily than hydroxyl group dissociation in the unmodified membranes.

To quantify the extent of TEMPO functionalisation, conductometric titration was conducted using 0.01 M NaOH as the titrant, monitoring the neutralisation of carboxylic acid groups (Fig. S5, SI). Each carboxylic group contributes one negative charge, allowing direct calculation of the surface charge density (σ). Pristine RC membranes showed a baseline

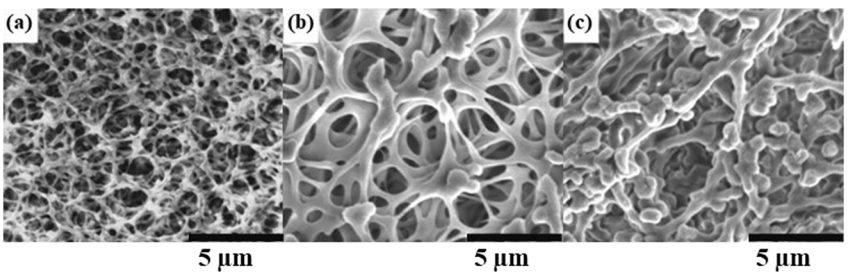

Fig. 1 SEM surface morphology of pristine RC membranes with nominal pore sizes of (a) 200 nm (RC-200), (b) 450 nm (RC-450) and (c) 1 μm (RC-1k). Scale bar = 5 μm.

acid group content of ~0.09 mmol g^{-1}. After TEMPO oxidation, this value increased elevenfold, reaching ~1.00 mmol g^{-1} across all three membrane types (RC-200, RC-450, and RC-1k), confirming the successful introduction of high-density carboxyl functionality.

In contrast, positively charged quaternary ammonium groups were introduced *via* an etherification reaction with CHMAC (see Scheme S1(b), in SI). RC membranes were reacted with CHMAC at 65 °C for 16 h, resulting in a significant shift in surface charge.[35] The zeta potential increased from −17.4 ± 0.4 mV to +10.0 ± 0.4 mV for RC-200, +12.4 ± 0.4 mV for RC-450, and +12.9 ± 0.7 mV for RC-1k (measured in 0.01 wt% solution at pH ~8). These results confirm the successful incorporation of quaternary ammonium groups and demonstrate that both negatively and positively charged functionalities can be effectively grafted onto RC membranes through targeted surface modification.

As CHMAC functionalisation does not introduce acidic groups, conductometric titration, used for quantifying carboxyl content in TEMPO-functionalised membranes, was not applicable. Instead, XPS was employed to quantify the incorporation of quaternary ammonium groups. As each CHMAC unit contains a single nitrogen atom bearing one unit of fixed positive charge, nitrogen content serves as a direct indicator of the extent of functionalisation. Survey and high-resolution XPS spectra of both pristine and CHMAC-functionalised membranes are shown in Fig. 2, S6 and S7 (SI). As expected, pristine RC membranes exhibited only carbon (C 1s) and oxygen (O 1s) peaks, with no detectable nitrogen signal. Following CHMAC modification, a distinct N 1s peak appeared, confirming the successful grafting of quaternary ammonium functionalities. Quantitative analysis of the nitrogen signal revealed increasing nitrogen content with pore size: 1.2 at% for CHMAC-RC-200, 1.5 at% for CHMAC-RC-450, and 2.2 at% for CHMAC-RC-1k. This trend reflects the enhanced accessibility of internal fibre surfaces in membranes with larger pore diameters, enabling greater incorporation of functional groups. Consequently, CHMAC-RC-1k exhibited the highest nitrogen content and, by extension, the most significant surface charge density among the samples tested.

Surface characterisation of functionalised RC membranes

FTIR spectroscopy was used to confirm the chemical composition of both pristine and functionalised RC membranes, as shown in Fig. 3 and S8 (SI). The FTIR spectra of pristine RC membranes exhibit characteristic cellulose peaks, including broad bands at 3492 cm^{-1} and 3444 cm^{-1} attributed to O–H stretching vibrations involved in hydrogen bonding (Fig. 3(a)). A distinct –OH stretching vibration appears at 3356 cm^{-1}, while the C–H stretching of aliphatic groups is observed at 2894 cm^{-1}. Additional key features include a C–O stretching vibration at 1644 cm^{-1}, O–H bending modes at 1367 cm^{-1} and 1316 cm^{-1}, and a prominent band at 894 cm^{-1}, corresponding to the C–O–C stretching of β-glycosidic linkages between glucose units in the cellulose backbone.[38]

Following functionalisation, distinct spectral changes were observed in the FTIR spectra of RC membranes. For CHMAC-functionalised membranes (CHMAC-RC-200), the emergence of a peak at 1476 cm^{-1} corresponds to the H–C–H bond of the quaternary ammonium moiety, confirming successful grafting of the cationic substituent.[39] However, this FTIR peak for CHMAC-RC is subtle, but consistent with the literature report.[39] The intensity is relatively low as the total number of CHMAC groups introduced is small compared to the cellulose backbone. Because of this, to further confirm CHMAC functionalisation, XPS analysis was undertaken (Fig. 2a and b). The XPS demonstrates a new Nitrogen peak absent in pristine, confirming the CHMAC attachment. Additionally, the high-resolution XPS analysis in the C 1s (275–300 eV) and O 1s (525–540 eV) regions revealed peak shifts upon CHMAC modification, further supporting the successful covalent attachment of quaternary ammonium groups to the cellulose backbone (Fig. S9, SI). Furthermore, the zeta potential measurement, which reveals a shift from negative to positive zeta potential values with CHMAC-functionalisation, collectively evidences the grafting of CHMAC onto cellulose.

In TEMPO-functionalised membranes (TEMPO-RC-200), a new absorption band at 1727 cm^{-1}, attributed to the C=O stretching vibration of carboxylic acid groups, confirms the oxidation of hydroxyl functionalities (Fig. 3(b)). Similar characteristic peaks were also observed for functionalised RC-450 and RC-1k membranes (Fig. S8, SI). The carboxyl gives rise to

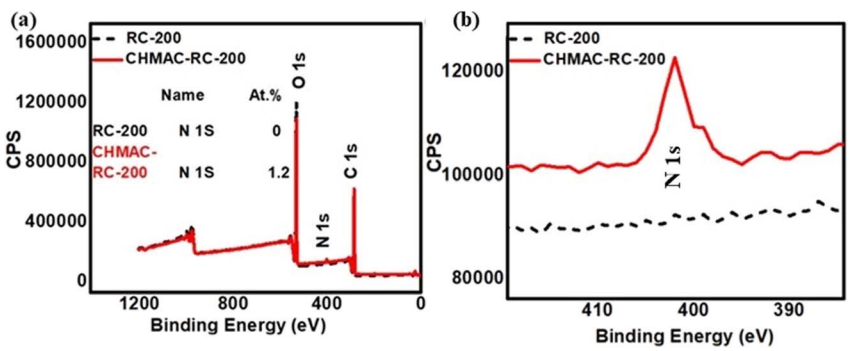

Fig. 2 (a) Survey XPS spectra of representative RC-200 membranes before and after functionalisation with CHMAC, including a summary of N 1s at% quantification. (b) The 390–415 eV region's high-resolution spectrum shows the N 1s peak.

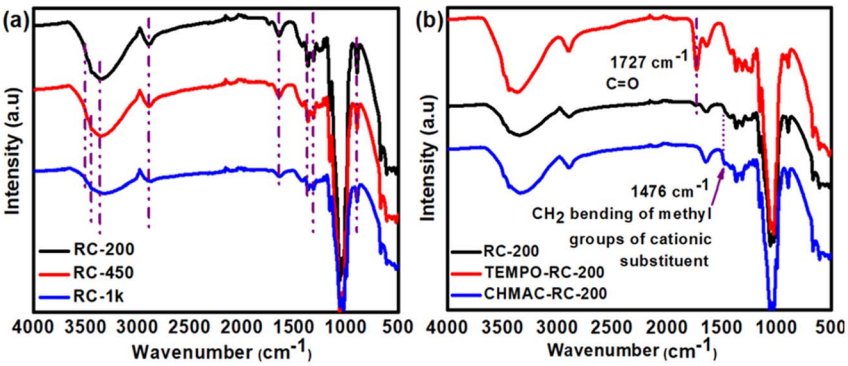

Fig. 3 FTIR spectra of (a) pristine RC membranes: RC-200 (black), RC-450 (red), and RC-1k (blue); and (b) RC-200 before (black) and after functionalisation with TEMPO (red) and CHMAC (blue).

strong peaks in the 1600–1750 region,[40] producing a more indicative spectral shift compared to CHMAC functionalisation.

Water contact angle measurements were conducted to evaluate changes in surface wettability upon functionalisation and to provide indirect evidence of successful chemical modification. Pristine RC membranes exhibited contact angles of 35.9 ± 0.7° for RC-200 and 29.3 ± 1.2° for RC-450, indicating increasing hydrophilicity with larger pore sizes. Following TEMPO oxidation, contact angles increased modestly to 40.6 ± 2.1° (TEMPO-RC-200) and 42.1 ± 1.2° (TEMPO-RC-450). This slight increase reflects the replacement of hydroxyl groups with carboxyl groups *via* TEMPO oxidation. While carboxyl groups remain hydrophilic, they reduce the density of hydroxyl functionalities on the surface, potentially altering surface energy and hydrogen bonding, which leads to a modest increase in the contact angle.[41] The contact angle measurements for both pristine and TEMPO-functionalised RC-1k could not be accurately obtained, as the highly porous hydrophilic structure acts like a sponge, quickly absorbing the droplet. CHMAC functionalisation resulted in a significant increase in contact angle, consistent with increased hydrophobicity due to the grafting of bulky (2-hydroxypropyl)trimethylammonium groups. Contact angles rose to 63.3 ± 2.1° for CHMAC-RC-200, 64.8 ± 2.6° for CHMAC-RC-450, and 70.7 ± 2.3° for CHMAC-RC-1k. The highest contact angle in RC-1k is attributed to both its larger pore diameter and higher CHMAC grafting density, as confirmed by nitrogen content in XPS analysis. These results confirm the successful and tuneable functionalisation of RC membranes, enabling control over surface polarity and wettability. To further assess chemical stability, functionalised membranes were stored in 1 M NaOH, 1 M HCl, and water for over 30 days, during which no delamination or visible degradation was observed, confirming their robustness in both acidic and basic environments. Additionally, thermal stability tests conducted by heating the membranes up to 30° above room temperature revealed no visible changes or disruption, indicating their robustness under mild thermal stress.

Ionic transport behaviour of electrolyte-infiltrated RCs

In nanofluidic membranes, ionic conductivity is predominantly governed by surface charge and pore size distribution, particularly at low electrolyte concentrations.[9,12] At concentrations $\leq 10^{-3}$ M, the influence of surface charge becomes dominant, as ion transport is confined to the electrical double layer (EDL) region near the membrane surface. In contrast, at higher concentrations, bulk electrolyte conductance prevails due to the screening of surface effects.[12] To investigate this behaviour, ionic conductivity measurements were performed on pristine and functionalised RC membranes using a nanofluidic device setup (Fig. S10, SI). Membranes were infiltrated with aqueous HCl at varying concentrations (10^{-5} to 10^{-2} M), and conductivity was recorded as a function of electrolyte concentration. The experimental data, plotted in Fig. 4(a) and (b), exhibit two distinct regimes: a plateau region at low concentrations ($<10^{-3}$ M), where conductivity remains relatively constant and deviates from bulk values, and a transition region beyond 10^{-3} M, where conductivity begins to approach bulk behaviour. This two-phase response is characteristic of nanofluidic systems dominated by surface-charge-governed transport in the low-concentration regime.[9]

Unmodified cellulose membranes carry a weakly negative surface charge due to the limited dissociation of surface hydroxyl groups, resulting in low ionic conductivity (~0.0015 ± 0.0004 mS cm^{-1}) across all pore sizes. This baseline surface charge was selectively enhanced in opposite directions through chemical functionalisation: oxidation with TEMPO introduced negatively charged carboxyl groups, while CHMAC grafting introduced positively charged quaternary ammonium groups. To quantify the effective fixed surface charge density (σ_s) introduced by functionalisation, zeta potential measurements were performed in 10^{-4} M HCl (pH ≈ 4), and the results were used to calculate σ_s *via* the Grahame equation (eqn (3)). This relationship links the zeta potential (ζ, in V) to surface charge under the assumption of a symmetric 1 : 1 electrolyte and a diffuse double-layer regime (see Table S1, SI).[42,43]

$$\sigma_s = \sqrt{8\varepsilon\varepsilon_0 RTI}\sin h\left(\frac{zF\zeta}{2RT}\right) \quad (3)$$

where, ε is the dielectric constant of water (≈78.5), ε_0 is the vacuum permittivity (8.854×10^{-12} F m^{-1}), R is the universal gas constant (8.314 J K^{-1} mol^{-1}), T is the temperature (298 K), and I is the ionic strength (mol m^{-3}), calculated as shown in eqn

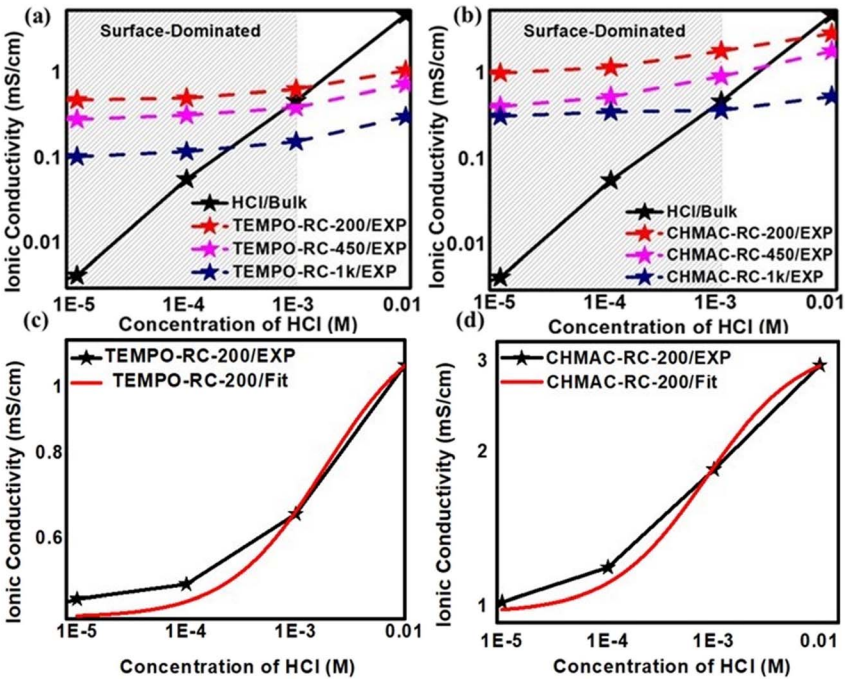

Fig. 4 Ionic conductivity of (a) TEMPO- and (b) CHMAC-functionalised RC membranes (RC-200, RC-450, and RC-1k) as a function of HCl concentration (10^{-5} to 10^{-2} M), measured using a nanofluidic conductivity device. The black line represents the theoretical bulk conductivity of the electrolyte; stars denote experimental data points, and dotted lines indicate the model fits. (c) and (d) show the modelled and experimental conductivity data for TEMPO- and CHMAC-functionalised RC-200 membranes, respectively, demonstrating close agreement with the fitted transport model. The red curves represent continuous fits using eqn (5).

(4) for a 1 : 1 electrolyte. z is the ionic valence (1 for H^+ or Cl^-), F is the Faraday constant (96 485 C mol^{-1}), and ζ is the zeta potential (in volts, converted from mV).

$$I = 2 \times 10^{-pH} \quad (4)$$

CHMAC-functionalised RC membranes exhibited positive zeta potentials in the range of +13 to +14 mV, corresponding to positive surface charge densities of approximately 0.013 to 0.016 mC m^{-2}. This behaviour is consistent with the successful incorporation of fixed quaternary ammonium groups, which impart a permanent positive charge and promote selective transport of chloride ions (Cl^-). In contrast, TEMPO-functionalised membranes displayed lower zeta potentials under acidic conditions (pH of 4) compared to those measured at a pH of 5, due to reduced dissociation of carboxylic acid groups at lower pH. Nevertheless, TEMPO-modified membranes maintained negative zeta potentials (−18 to −21 mV), translating to surface charge densities in the range of 0.019 to 0.022 mC m^{-2}. These values confirm the presence of carboxylate-rich surfaces capable of supporting efficient proton (H^+) conduction. A summary of these electrokinetic properties, alongside literature comparisons, is provided in Table S1 (SI).

To evaluate the influence of surface charge (modulated *via* TEMPO and CHMAC functionalisation) and pore size (200, 450, and 1000 nm) on nanofluidic conductivity, ionic conductivity measurements were conducted on functionalised RC membranes across a range of HCl concentrations (10^{-5} to 10^{-3} M), as summarised in Table 1. A substantial enhancement in conductivity was observed following functionalisation. For TEMPO-functionalised membranes, the most significant improvement, approximately 370-fold, was recorded for RC-200, while RC-1k exhibited a 90-fold increase. This enhancement is attributed to the introduction of negatively charged carboxylate groups through TEMPO-mediated oxidation. As reported by Li *et al.*[16] this functionalisation increases the cellulose surface charge by converting hydroxyl groups into carboxylic acids, which readily dissociate into carboxylate ions. The resulting negative electrostatic field facilitates selective ion transport by attracting counter-ions (H^+ from HCl) and repelling co-ions (Cl^-), leading to a charge-balanced environment within the nanochannels. This ion-selective transport mechanism enhances counter-ion mobility while suppressing co-ion diffusion, resulting in increased charge separation and higher effective conductivity compared to the bulk electrolyte. Therefore, the ionic conductivity in surface-functionalised RC membranes is predominantly governed by the surface charge density and its interaction with counter-ions in the electrolyte.

A comparable enhancement in ionic transport was observed for CHMAC-functionalised RC membranes, where the incorporation of 1.5–2.2 at% quaternary ammonium groups introduced a net positive surface charge.[35] These fixed cationic sites facilitate the selective migration of anions, *e.g.*, Cl^-, while hindering the transport of cations, resulting in ion-selective conductivity. This surface-driven selectivity led to a marked increase in ionic conductivity, with RC-200 exhibiting a 950-fold enhancement and RC-1k showing a 200-fold increase compared

Table 1 Ionic conductivity (κ) values of TEMPO- and CHMAC-functionalised RC membranes measured across a range of 10^{-5} to 10^{-3} M HCl using a nanofluidic conductivity setup. Values represent the surface-governed transport regime. Pristine RCs, ionic conductivity = ~0.0015 ± 0.0004 mS cm^{-1}

Membranes	Ionic conductivity (mS cm^{-1})	Membranes	Ionic conductivity (mS cm^{-1})
TEMPO-RC-200	0.55 ± 0.09	CHMAC-RC-200	1.41 ± 0.40
TEMPO-RC-450	0.34 ± 0.06	CHMAC -RC-450	0.63 ± 0.27
TEMPO-RC-1k	0.13 ± 0.03	CHMAC -RC-1k	0.35 ± 0.03

to their pristine counterparts. To the best of our knowledge, this represents one of the largest reported conductivity enhancements in biopolymer membranes under dilute, fully aqueous conditions, highlighting the impact of surface charge engineering on electrokinetic performance. These results confirm that increased surface charge density, whether positive or negative, substantially boosts nanofluidic conductivity across all pore sizes.

For both TEMPO- and CHMAC-functionalised membranes, ionic conductivity exhibited a consistent dependence on pore size. At comparable surface charge densities, conductivity followed the trend RC-200 > RC-450 > RC-1k, with respective enhancements of 370-, 220-, and 90-fold for TEMPO-functionalised membranes, and 950-, 420-, and 200-fold for CHMAC-functionalised membranes. This trend is characteristic of nanofluidic systems, where smaller pores enhance the influence of surface charge by confining the electrical double layer (EDL) and increasing the overlap between surface and bulk ionic regions.[9] However, the substantial ionic conductivity enhancements observed for CHMAC- and TEMPO-functionalised RC membranes, even at large nominal pore sizes, *e.g.*, 1 μm, suggest that classical pore size metrics may underestimate confinement effects. The fibrous, layered structure of RC membranes likely introduces significant tortuosity and a wide distribution of effective pore dimensions. These complex geometries may facilitate localised EDL overlap and maintain strong surface-governed ion transport over extended distances. As nominal pore size increases, however, EDL overlap decreases and the effect of surface charge becomes increasingly screened, leading to bulk-like behaviour in which ion motion is governed more by electrolyte concentration than by interfacial charge.[12] These findings, supported by data in Fig. 4 and Table 1, highlight the synergistic roles of surface charge density and pore architecture in modulating ion transport through functionalised RC membranes. To validate these observations under device-relevant conditions, ionic conductivity was independently measured using both linear sweep voltammetry (LSV) and electrochemical impedance spectroscopy (EIS). The two techniques yielded consistent results, with EIS-derived conductivities of 1.64 mS cm^{-1} for CHMAC-RC-200 and 0.58 mS cm^{-1} for TEMPO-RC-200, which closely matched the LSV-derived values (Table S2, SI; Fig. S11 and S12). This agreement confirms the robustness of both methods for assessing nanofluidic ionic conductivity of our system under low-concentration electrolyte conditions.

To further understand and quantify ion transport in functionalised RC membranes, we applied a phenomenological model adapted from nanofluidic literature to fit experimental ionic conductivity data as a function of HCl concentration, as shown in eqn (5):[4]

$$\kappa(c) = \frac{\kappa_{surf} + \mu_{eff} c}{1 + \frac{c}{c^*}} \quad (5)$$

where, $\kappa(c)$ is total ionic conductivity (mS cm^{-1}) and c is the bulk electrolytic concentration (M). The applied model effectively captures the transition from surface-dominated conduction at low electrolyte concentrations to bulk-governed transport at higher concentrations.[4] This behaviour arises from the screening of the surface charge by the electrical double layer (EDL) and has been widely used to describe nanofluidic ion transport in confined systems, including charged nanochannels and porous polymer membranes.[12,35]

By fitting this model to the experimental conductivity data for TEMPO- and CHMAC-functionalised RC membranes, three key transport parameters were extracted: surface conductivity (κ_{surf}), effective ion mobility (μ_{eff}), and the crossover concentration (c^*). Surface conductivity quantifies the membrane's ability to conduct ions *via* EDL-dominated pathways under low-concentration conditions.[44] Effective ion mobility reflects how rapidly ionic conductivity increases with electrolyte concentration, while the crossover concentration denotes the threshold at which surface-governed transport is overtaken by bulk conduction.[45] The fitted values for κ_{surf}, μ_{eff}, and c^* are summarised in Table 2, alongside literature benchmarks for comparable membrane systems. Representative model fits for RC-200 are shown in Fig. 4(c) and (d), while fitted results for all other membranes are provided in Fig. S13 (SI).

Consistent with experimental observations, model fitting revealed that CHMAC-RC-200 exhibited the highest surface conductivity (0.97 mS cm^{-1}) and effective ion mobility (2119 mS cm^2 mol^{-1}), along with a low crossover concentration of 1.5 mM. These values indicate dominant surface-governed transport and efficient anion mobility even at low electrolyte concentrations. In contrast, TEMPO-functionalised membranes showed moderate surface conductivities and higher crossover concentrations, reflecting weaker electrostatic interactions with chloride ions. These trends highlight the impact of both surface functionalisation type and pore size on membrane performance, with smaller pores enhancing nanofluidic effects, a finding consistent with the experimental and fitted data presented in Fig. 4. Significantly, the extracted surface conductivity

Table 2 Surface conductivity (κ_{surf}), effective ion mobility (μ_{eff}), and crossover concentration (c^*) of TEMPO- and CHMAC-functionalised RC membranes obtained from ionic conductivity model fitting

Membrane	κ_{surf} (mS cm^{-1})	μ_{eff} (mS cm^2 mol^{-1})	c^* (mM)	References
CHMAC-RC-200	0.97	2119	1.53	This work
CHMAC-RC-450	0.42	929	2.34	This work
CHMAC-RC-1k	0.33	134	4.87	This work
TEMPO-RC-200	0.46	412	3.07	This work
TEMPO-RC-450	0.28	203	4.78	This work
CHMAC modified bacterial cellulose membrane	0.42 – unaligned membrane	N/A	N/A	35
	1.2 – aligned membrane	N/A	N/A	
TEMPO oxidised bacterial cellulose	0.35	N/A	N/A	46

and ion mobility values remain high across all pore sizes, which may be attributed to the intrinsic structural disorder of the RC matrix. Rather than behaving as uniformly porous membranes, the overlapping cellulose fibres create anisotropic and irregular nanochannels. This network can impose ion pathway distortion and channel narrowing, reinforcing surface-charge effects in regions of local confinement. The differences in conductivity behaviour can be further rationalised by considering the acid-base properties of the introduced functional groups. TEMPO oxidation yields carboxylic acid (-COOH) groups with a typical pK_a of 4.5–5.0. Under the experimental conditions (HCl concentrations from 10^{-5} to 10^{-2} M), the local pH remains below the pK_a, resulting in predominantly protonated, neutral carboxyl groups. Consequently, these groups contribute minimally to fixed surface charge, accounting for the relatively lower κ_{surf} and μ_{eff} values observed in TEMPO-functionalised membranes.

In contrast, CHMAC functionalisation introduces quaternary ammonium groups ($-N^+R_3$), which are permanently cationic and retain their charge independent of the surrounding pH. This fixed positive charge establishes a stable electrostatic field that facilitates the selective migration of anions such as Cl^-. Consequently, CHMAC-RC membranes, particularly RC-200, exhibited the highest surface conductivity and effective ion mobility among all tested samples. This behaviour aligns with classical nanofluidic theory, wherein fixed surface charges dominate ion transport under low ionic strength conditions. The observed differences between TEMPO- and CHMAC-modified systems highlight the importance of considering the acid-base characteristics (pK_a/pK_b) of surface functional groups when designing materials for specific electrolyte environments. In particular, the use of permanently charged moieties such as quaternary ammonium groups offers a distinct advantage for enhancing ionic transport in acidic or electrostatically screened systems.

The ionic conductivity values and transport parameters obtained for CHMAC-functionalised RC membranes compare favourably with those reported for other functionalised membranes and nanofluidic systems in recent literature. For example, CHMAC-RC-200 achieved an ionic conductivity of ~3 mS cm^{-1} at 10^{-2} M HCl and maintained values above 1 mS cm^{-1} even at 10^{-5} M, demonstrating efficient ion transport sustained across a wide concentration range. In contrast, Wu *et al.*[35] reported ionic conductivities of ~0.42 mS cm^{-1} for unaligned CHMAC-functionalised bacterial cellulose in 10^{-3} to 10^{-6} M KCl, which is lower than the conductivities achieved here. This suggests that regenerated cellulose provides a higher density of accessible surface sites and superior ion mobility, likely due to its open, hydrated fibre network. Notably, the membranes tested in this study maintain high ionic conductivity under ambient, low-concentration aqueous conditions without the need for specialised solvents or environmental control. The ionic conductivity measured for the TEMPO-oxidised cellulose membranes is consistent with values reported in some studies;[46] however, higher ionic conductivities have been documented for other TEMPO-oxidised cellulose systems.[16,35,47] The comparatively lower conductivity observed in our membranes, as discussed earlier, may be attributed to the use of an acidic electrolyte with a pH significantly below the pK_a (10^{-5} to 10^{-2} M), which results in the carboxyl groups remaining predominantly in their neutral acid form, thereby reducing the overall negative charge density.

Ionic thermoelectric properties

Membranes with high surface charge density, enhanced ionic conductivity, and strong ion selectivity are well-suited for thermally driven energy harvesting applications. In this study, TEMPO and CHMAC functionalisation significantly increased the surface charge of regenerated cellulose (RC) membranes, thereby improving their ionic conductivity and selective ion

Table 3 Seebeck coefficient (S) values of functionalised RCs

Membranes	S (mV K^{-1})	Membranes	S (mV K^{-1})	Membranes	S (mV K^{-1})
RC-200	-0.35 ± 0.05	TEMPO-RC-200	-1.13 ± 0.06	CHMAC-RC-200	3.41 ± 0.24
RC-450	-0.13 ± 0.02	TEMPO -RC-450	-0.87 ± 0.04	CHMAC-RC-450	1.1 ± 0.18
RC-1k	-0.09 ± 0.15	TEMPO -RC-1k	-0.36 ± 0.01	CHMAC -RC-1k	1.05 ± 0.17

Table 4 Ionic thermoelectric properties of RC-based membranes at 10^{-4} M HCl

Membrane	S (mV K^{-1})	κ (mS m^{-1})	PF (μW m^{-1} K^{-2})
RC-200	−0.35	5.73	0.00
TEMPO-RC-200	−1.13	51.43	0.06
CHMAC-RC-200	+3.41	118.90	1.38
RC-450	−0.13	5.73	0.00
TEMPO-RC-450	−0.87	32.44	0.02
CHMAC-RC-450	+1.1	54.15	0.07
RC-1k	−0.09	5.73	0.00
TEMPO-RC-1k	−0.36	12.10	0.00
CHMAC-RC-1k	+1.05	36.14	0.04

transport characteristics (see Tables 3, 4 and Fig. 5). These enhancements suggest that functionalised RC membranes are promising candidates for use in ionic thermoelectric (i-TE) devices that convert low-grade thermal energy into electrical output. To evaluate their suitability, the ionic thermoelectric behaviour of the membranes was examined by analysing their thermal charging response under controlled temperature gradients.

In-plane ionic thermoelectric characterisation

To assess their ionic thermoelectric performance, the membranes were infiltrated with 10^{-4} M HCl and positioned between two gold-coated silicon wafers (Fig. S1, SI). A Peltier element was used to heat and cool the system alternately, generating a controlled temperature gradient in 2 °C increments, up to a maximum of 10 °C. The resulting thermal charging behaviour is shown in Fig. 5(a)–(c), S14, and S15 (SI). The corresponding Seebeck coefficient, S for each membrane was calculated and summarised in Table 3.

Surface functionalisation significantly increased the Seebeck coefficient of the RC membranes. Both TEMPO and CHMAC modifications enhanced the fixed surface charge, negative in the case of TEMPO and positive for CHMAC, thereby improving ion selectivity. Similar to electrophoresis, membranes with higher ion selectivity enable more effective ion separation during thermophoresis. This selective ion transport enhances asymmetry in charge carrier distribution under a thermal gradient, leading to an increase in Seebeck coefficient.[48] TEMPO functionalisation of RCs of different pore sizes led to an average seven-fold increase in thermoelectric voltage compared to pristine RC membranes. In contrast, CHMAC-functionalised membranes RCs (250, 450, and 1000 nm) exhibited an even greater enhancement, approximately twelve-fold, relative to both pristine and TEMPO-modified samples. Moreover, as the pore sizes increase, for both TEMPO and CHMAC functionalisation, the Seebeck coefficient values decrease. This trend closely aligns with that of ionic conductivity, reinforcing the connection between conductivity, ion selectivity, and thermoelectric performance. This reduction in performance with increasing pore size highlights the growing dominance of bulk transport over surface conduction, as larger pores diminish the influence of surface charge relative to the total cross-sectional area available for ion transport. This observation underscores the critical role of nanoscale confinement in maintaining surface-charge-governed transport and enhancing thermoelectric output, with smaller pore sizes proving more efficient for ionic thermoelectrics. Both pristine and TEMPO-RC

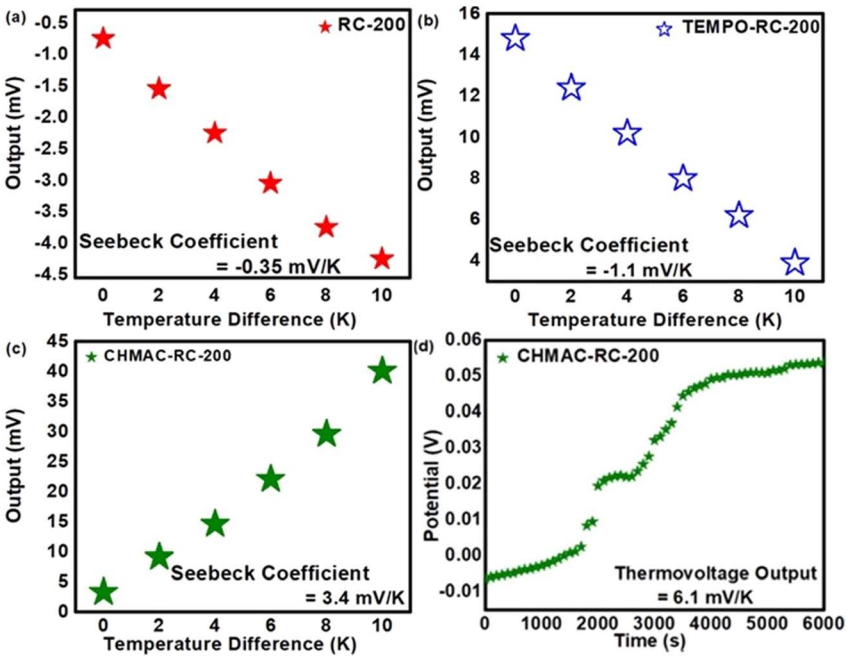

Fig. 5 Thermal charging behaviour of RC-200 membranes: (a) pristine, and (b and c) TEMPO- and CHMAC-functionalised RC-200 under incremental 2 °C temperature steps from room temperature. (d) Open-circuit voltage response of a stacked (sandwich-type) CHMAC-RC-200 cell under a 10 K temperature gradient.

membranes possess negatively charged surfaces and display similar cation-selective transport characteristics under a thermal gradient. In contrast, CHMAC-functionalised membranes, bearing a permanent positive surface charge, exhibit anion-selective behaviour, resulting in a reversed thermovoltage polarity.[35] This difference in thermopower sign, as reported in Table 4, supports the distinct ion transport mechanisms, proton (H^+) migration for negatively charged membranes and chloride (Cl^-) migration for positively charged ones. To evaluate overall thermoelectric performance, the Seebeck coefficient (S) and ionic conductivity (κ) were used to calculate the power factor (PF) at a fixed electrolyte concentration of 10^{-4} M HCl.[22] The thermoelectric parameters for all membranes are summarised in Table 4.

The thermoelectric performance of the functionalised cellulose membranes in 10^{-4} M HCl is summarised in Table 4. Among all samples, CHMAC-RC-200 exhibited the highest Seebeck coefficient (S), reaching +3.41 mV K^{-1}, which surpasses values previously reported for comparable cellulose-based systems.[33,49] This elevated S, combined with enhanced ionic conductivity (κ), results in markedly improved power factors (PF), underscoring the effectiveness of surface functionalisation strategies in tuning thermoelectric properties. Additionally, the thermoelectric figure of merit (ZT) was estimated at a constant thermal conductivity of 0.5 W m^{-1} K^{-1} and a temperature of 298 K, based on reported values for hydrated cellulose membranes.[50,51] While thermal conductivity can vary with porosity, pore structure, and surface functionalisation, this representative value was selected to avoid overestimation. For the best performing CHMAC-RC-200 membranes, an ionic figure of merit, ZT of 8.24×10^{-4} was obtained in comparison to 4.18×10^{-7} for pristine RC-200.

The exclusive use of an aqueous acidic electrolyte offers multiple advantages: it is environmentally benign, cost-effective, and maintains membrane integrity and ion mobility, thereby enabling consistent thermovoltage generation. These findings demonstrate that functionalised cellulose membranes, when paired with dilute aqueous electrolytes, offer a sustainable and high-performing alternative to conventional synthetic thermoelectric materials, particularly under low-concentration and low-grade thermal conditions.

Cross-plane thermoelectric characterisation

To evaluate ionic thermoelectric behaviour in the through-thickness direction, we employed a stacked membrane configuration, commonly used in prior studies to characterise perpendicular Seebeck response under a thermal gradient.[52–54] This setup was selected over the in-plane geometry to mitigate any issue arising from water evaporation. In the in-plane configuration, exposure to ambient conditions can lead to electrolyte drying, resulting in unstable ion concentrations, disrupted thermal gradients, and suppressed thermovoltage output. By contrast, the stacked (sandwich-type) cell design confines the electrolyte, ensuring continuous hydration and thereby preserving ionic transport while enhancing thermoelectric stability. In this setup, ten RC-200 membranes (each ~40 μm thick) were stacked between gold-coated silicon wafers and infiltrated with 10^{-4} M HCl (Fig. S2, SI). The assembled stack was tested using a modified ASTM D5470-06 apparatus,[37] in which a different temperature gradient was applied using a Peltier element and a controlled heat source. Local temperatures were monitored *via* embedded thermistors to ensure accurate temperature gradient measurements across the membrane stack.

Under these conditions, the pristine RC-200 membrane stack produced an open-circuit voltage of −6 mV, corresponding to a thermal gradient ratio of −0.6 mV K^{-1}. Functionalisation with TEMPO enhanced the output to −23 mV (−2.3 mV K^{-1}), representing a 3.8-fold increase. The highest performance was observed for CHMAC-RC-200, which yielded +61 mV under the same thermal gradient, corresponding to +6.1 mV K^{-1}, a 10-fold improvement over the pristine membrane (Fig. 5(d)).

For comparison, the in-plane Seebeck coefficients for the same membranes were −0.35 mV K^{-1} (RC-200), −1.13 mV K^{-1} (TEMPO-RC-200), and +3.41 mV K^{-1} (CHMAC-RC-200). The enhanced performance in the stacked configuration is attributed to improved hydration retention, reduced evaporative loss, and enhanced thermal and electrochemical coupling through the membrane thickness.

Significantly, the total thermovoltage did not scale linearly with the number of membranes, as might be expected in solid-state thermoelectrics. In ionic systems, the Seebeck coefficient is sensitive to ionic redistribution, interfacial potential barriers, and electrolyte polarisation across junctions.[48,55] These non-idealities resulted in sub-linear scaling in our stacked assemblies. Specifically, while a 10-layer CHMAC-RC-200 stack would ideally yield ~34 mV K^{-1} based on the in-plane value, the measured value was 6.1 mV K^{-1}. Estimated interfacial losses per membrane were approximately 17–18% for RC-200, 6–8% for TEMPO-RC-200, and 10–12% for CHMAC-RC-200. The slightly higher loss in CHMAC-functionalised membranes may be attributed to reduced wettability and increased interfacial resistance due to the hydrophobic quaternary ammonium groups.

Despite these challenges, the thermoelectric performance of CHMAC-RC-200 remains among the highest reported for biopolymer-based i-TE systems operating under ambient conditions. For comparison, bacterial cellulose/boron nitride composites achieved Seebeck coefficients of 0.52–0.74 mV K^{-1} under a 50 K gradient,[33] while a transparent paper-based TEG produced 2.3 mV K^{-1} under a 10 K body heat gradient.[56] A MWCNT-carbonised cellulose nanofiber composite yielded a Seebeck coefficient of just 12 μV K^{-1}, even under a 70 °C temperature difference.[57] In contrast, the CHMAC-RC-200 system presented here delivered +6.1 mV K^{-1} using only dilute aqueous electrolyte and low-grade heat. These results demonstrate the promise of surface-engineered regenerated cellulose membranes as scalable, eco-friendly platforms for efficient ionic thermoelectric energy harvesting.

Although ZT for aqueous ionic systems remain lower than that of electronic counterparts,[58] this limitation is inherent to all ionic thermoelectric materials due to the significantly lower ionic conductivity compared to electronic conductivity.

Nevertheless, since ions can carry substantial entropy changes, ionic thermoelectric systems often exhibit a high thermovoltage output. In this work, we demonstrate effective and facile functionalisation strategies on regenerated cellulose membrane systems, offering advantages such as low cost, eco-compatibility, and mechanical flexibility, making them suitable for niche applications like on-body ionic thermoelectric systems, temperature sensors, and for green energy harvesting, where modest voltage output is sufficient, but sustainability is key. To further improve the thermoelectric performance obtained, several strategies could be explored. Improving interfacial adhesion, either through chemical crosslinking or controlled mechanical compression, may reduce ionic discontinuities and interfacial resistance.[52–54] Incorporating intermediate electrolyte layers or engineering wettability gradients, *e.g.*, alternating hydrophilic and hydrophobic domains, could facilitate continuous ion transport across membrane interfaces.[16] Additionally, employing asymmetric surface functionalisation, where adjacent membranes carry opposite surface charges, may promote directional ion migration and enhance thermovoltage generation through internal ionic rectification. Future exploration of membranes with ≤100 nm porosity—either through custom fabrication or advanced processing—may provide further performance enhancement due to more substantial surface charge effects and increased ion–wall interactions in confined domains. However, identifying an optimal pore size requires balancing the increased hydraulic resistance, reduced permeability, and structural challenges, particularly in soft biopolymer systems, to achieve increased performance.[59] For the dilute monovalent electrolytes investigated here, 200 nm membranes demonstrated the most effective between surface-governed transport and membrane integrity. In addition, the degree of surface functionalisation is an important factor influencing membrane performance. A higher density of surface functional groups provides an increased surface charge, thereby enhancing both ionic conductivity and thermoelectric output. And the efficiency of the surface functionalisation can itself be affected by the membrane's pore size. In our CHMAC-functionalised membranes, XPS analysis revealed a higher nitrogen content in samples with larger pore sizes, indicating a more effective functionalisation. This is due to the steric hindrance, which restricts the ability of bulky functional groups such as CHMAC to diffuse into narrower nanochannels and effectively attach to the internal surface.[60,61] In contrast, wider pores provide greater accessibility of internal surface sites. Therefore, while smaller pores enhance confinement effects, larger pores may provide more accessible surface area for efficient chemical functionalisation, further influencing the overall ion transport behaviour. The combined effect of pore size on both surface charge regulation and mechanical stability must therefore be carefully considered during device optimisation, and further research guided by electrolyte-membrane specific modelling may help optimise performance in future systems. Collectively, these approaches offer promising routes to increase the efficiency of nanofluidic ionic thermoelectric generators based on sustainable materials such as regenerated cellulose.

Conclusions

This study demonstrates that the surface charge density of RC membranes with varying pore sizes can be substantially enhanced through targeted chemical functionalisation. TEMPO-mediated oxidation converted hydroxyl groups into carboxyl groups, increasing negative surface charge by approximately eleven-fold. Conversely, etherification with CHMAC introduced fixed quaternary ammonium groups, yielding positive surface charge densities ranging from 1.2 to 2.2%, as confirmed by XPS analysis. Ionic conductivity measurements in HCl electrolytes of varying concentrations revealed that conductivity scales directly with surface charge and inversely with pore size. TEMPO functionalisation enhanced ionic conductivity by a factor of 90 to 370, while CHMAC functionalisation resulted in even greater improvements, ranging from 200- to 950-fold depending on membrane pore size. Thermoelectric performance followed a similar trend. TEMPO-functionalised membranes exhibited 3- to 7-fold increases in thermovoltage, while CHMAC-functionalised membranes achieved 8- to 12-fold enhancements. Among all tested systems, CHMAC-RC-200, with a surface ammonium content of 1.2%, demonstrated the highest performance, achieving a Seebeck coefficient of +3.41 mV K^{-1} in the in-plane configuration and a power factor of 1.38 μW m^{-1} K^{-2}. When ten of these membranes were stacked in a sandwich-style configuration and infiltrated with 10^{-4} M HCl, the system generated a peak thermovoltage output of +6.1 mV K^{-1}. In summary, this work highlights the critical role of surface charge engineering and pore architecture in tuning ionic transport and thermoelectric response in biopolymer membranes. In addition, the unexpected magnitude of conductivity enhancement in membranes with large nominal pore sizes suggests that the internal fibrous structure introduces significant tortuosity and non-uniform channel geometries. These features likely enhance ion–surface interactions and contribute to the surface-governed transport regime observed, even at sub-microscale pore diameters. While the overall *ZT* is lower than traditional thermoelectric devices, the aqueous compatibility, scalability, and non-toxic nature of the material position them well for alternative applications such as flexible wearable electronics, sensors, thermal detectors, and as green energy harvesters for environmental monitoring, where safety and sustainability are key. Collectively, these insights establish regenerated cellulose membranes as a versatile and eco-conscious platform for advancing thermoelectrics beyond energy harvesting, with strong potential for next-generation flexible and bio-integrated electronics. Future studies will focus on evaluating the long-term thermal and operational stability of systems under cyclic temperature gradients for real-world deployment.

Author contributions

Anjali Ashokan: conceptualisation, methodology development, investigation, formal analysis, validation, writing – original draft, writing – review & editing. Kamil Rahme: conceptualisation, methodology development, supervision. Rupa Ranjani

Palanisamy: methodology development, formal analysis. N. Padmanathan: methodology development, formal analysis. Kafil M. Razeeb: supervision, writing – review & editing, resources, validation. Subhajit Biswas: formal analysis, writing – review & editing, supervision, validation. Justin D. Holmes: formal analysis, writing – review & editing, supervision, resources, validation.

Conflicts of interest

There are no conflicts to declare.

Data availability

The datasets generated during and/or analysed during the current study are available in the TRANSLATE Zenodo repository, **https://zenodo.org/communities/translateh2020/**.

Supplementary information is available. See DOI: **https://doi.org/10.1039/d5ta05281e**.

Acknowledgements

This research is supported by Irish Government funding *via* the DAFM NXTGENWOOD research program (grant agreement: 2019PROG704), and by European Union's Horizon 2020 research and innovation programme under grant agreement number 964251 (TRANSLATE). The authors also wish to acknowledge Dr Fathima Laffir at the Bernal Institute at University of Limerick for XPS analysis. They also thank Dr Ievgen Nedrygailov and Dr Mehran Nozari Asbemarz for their valuable discussions on electrochemistry.

References

1 S. Karki, G. Hazarika, D. Yadav and P. G. Ingole, *Desalination*, 2024, **573**, 117200.
2 H. Strathmann, A. Grabowski and G. Eigenberger, *Ind. Eng. Chem. Res.*, 2013, **52**, 10364–10379.
3 L. Dai, F. Xu, K. Huang, Y. Xia, Y. Wang, K. Qu, L. Xin, D. Zhang, Z. Xiong, Y. Wu, X. Guo, W. Jin and Z. Xu, *Angew. Chem., Int. Ed.*, 2021, **60**, 19933.
4 A. Siria, P. Poncharal, A. L. Biance, R. Fulcrand, X. Blase, S. T. Purcell and L. Bocquet, *Nature*, 2013, **494**, 455–458.
5 J. Feng, M. Graf, K. Liu, D. Ovchinnikov, D. Dumcenco, M. Heiranian, V. Nandigana, N. R. Aluru, A. Kis and A. Radenovic, *Nature*, 2016, **536**, 197–200.
6 N. Van Toan, M. M. I. M. Hasnan, D. Udagawa, N. Inomata, M. Toda, S. M. Said, M. F. M. Sabri and T. Ono, *Energy Convers. Manage.*, 2019, **199**, 111979.
7 N. An, A. M. Fleming, H. S. White and C. J. Burrows, *Proc. Natl. Acad. Sci. U. S. A.*, 2012, **109**, 11504–11509.
8 Y. Li, C. Li, S. Li, B. Su, L. Han and B. Mandal, *J. Mater. Chem. A*, 2019, **7**, 13315–13330.
9 M. Wang, Q. Kang and E. Ben-Naim, *Anal. Chim. Acta*, 2010, **664**, 158–164.
10 K. L. Jensen, J. T. Kristensen, A. M. Crumrine, M. B. Andersen, H. Bruus and S. Pennathur, *Phys. Rev. E*, 2011, **83**, 056307.
11 G. V. Franks and Y. Gan, *J. Am. Ceram. Soc.*, 2007, **90**, 3373–3388.
12 D. Stein, M. Kruithof and C. Dekker, *Phys. Rev. Lett.*, 2004, **93**, 035901.
13 J. J. Shao, K. Raidongia, A. R. Koltonow and J. Huang, *Nat. Commun.*, 2015, **6**, 7602.
14 W. Xian, X. Zuo, C. Zhu, Q. Guo, Q. W. Meng, X. Zhu, S. Wang, S. Ma and Q. Sun, *Nat. Commun.*, 2022, **13**, 3386.
15 Z. Q. Li, Z. Q. Wu, X. L. Ding, M. Y. Wu and X. H. Xia, *CCS Chem.*, 2021, **3**, 2174–2182.
16 T. Li, X. Zhang, S. D. Lacey, R. Mi, X. Zhao, F. Jiang, J. Song, Z. Liu, G. Chen, J. Dai, Y. Yao, S. Das, R. Yang, R. M. Briber and L. Hu, *Nat. Mater.*, 2019, **18**, 608–613.
17 N. Van Toan, T. T. K. Tuoi, N. Inomata, M. M. I. M. Hasnan, M. Toda, I. Voiculescu, S. M. Said and T. Ono, *Energy Convers. Manage.*, 2022, **264**, 115760.
18 S. W. Lee, Y. Yang, H. W. Lee, H. Ghasemi, D. Kraemer, G. Chen and Y. Cui, *Nat. Commun.*, 2014, **5**, 3942.
19 M. Rahimi, A. P. Straub, F. Zhang, X. Zhu, M. Elimelech, C. A. Gorski and B. E. Logan, *Energy Environ. Sci.*, 2018, **11**, 276–285.
20 X. Wang, Y. T. Huang, C. Liu, K. Mu, K. H. Li, S. Wang, Y. Yang, L. Wang, C. H. Su and S. P. Feng, *Nat. Commun.*, 2019, **10**, 4151.
21 K. D. Sandbakk, A. Bentien and S. Kjelstrup, *J. Membr. Sci.*, 2013, **434**, 10–17.
22 F. Jiao, A. Naderi, D. Zhao, J. Schlueter, M. Shahi, J. Sundström, H. Granberg, J. Edberg, U. Ail, J. Brill, T. Lindström, M. Berggren and X. Crispin, *J. Mater. Chem. A*, 2017, **5**, 16883–16888.
23 V. M. Barragán, K. R. Kristiansen and S. Kjelstrup, *Entropy*, 2018, **20**(12), 905.
24 T. J. Konch, R. K. Gogoi, A. Gogoi, K. Saha, J. Deka, K. A. Reddy and K. Raidongia, *Mater. Chem. Front.*, 2018, **2**, 1647–1654.
25 M. M. Rahman, *Membranes*, 2023, **13**(12), 164.
26 W. Zhang, Q. Zhao and J. Yuan, *Angew. Chem., Int. Ed.*, 2018, **57**, 6754.
27 X. C. Chen, H. Zhang, S. H. Liu, Y. Zhou and L. Jiang, *ACS Nano*, 2022, **16**, 17613–17640.
28 T. Li, C. Chen, A. H. Brozena, J. Y. Zhu, L. Xu, C. Driemeier, J. Dai, O. J. Rojas, A. Isogai, L. Wågberg and L. Hu, *Nature*, 2021, **590**, 47–56.
29 A. Barhoum, K. Deshmukh, M. L. García-Betancourt, S. Alibakhshi, S. M. Mousavi, A. Meftahi, M. S. K. Sabery and P. Samyn, *Carbohydr. Polym.*, 2023, **317**, 121057.
30 Y. H. Jung, T. H. Chang, H. Zhang, C. Yao, Q. Zheng, V. W. Yang, H. Mi, M. Kim, S. J. Cho, D. W. Park, H. Jiang, J. Lee, Y. Qiu, W. Zhou, Z. Cai, S. Gong and Z. Ma, *Nat. Commun.*, 2015, **6**, 7170.
31 G. A. Junter and L. Lebrun, *Rev. Environ. Sci. Biotechnol.*, 2017, **16**, 455–489.
32 M. Graf, M. Lihter, D. Unuchek, A. Sarathy, J.-P. Leburton, A. Kis and A. Radenovic, *Joule*, 2019, **3**(6), 1549–1564.

33 X. Jia, M. Zhang, Y. Zhang, Y. Fu, N. Sheng, S. Chen, H. Wang and Y. Du, *Nano Lett.*, 2024, **24**, 2218–2225.
34 T. Saito, S. Kimura, Y. Nishiyama and A. Isogai, *Biomacromolecules*, 2007, **8**, 2485–2491.
35 Z. Wu, P. Ji, B. Wang, N. Sheng, M. Zhang, S. Chen and H. Wang, *Nano energy*, 2021, **80**, 105554.
36 C. Wang, C. Miao, X. Zhu, X. Feng, C. Hu, D. Wei, Y. Zhu, C. Kan, D. Shi and S. Chen, *ACS Appl. Nano Mater.*, 2019, **2**, 4193–4202.
37 A. Tanwar, S. Lal, R. Kaur, N. Padmanathan, E. Dalton and K. M. Razeeb, *Appl. Therm. Eng.*, 2023, **224**, 120111.
38 N. S. N. Mazlan, S. Zakaria, S. Gan, C. C. Hua and K. W. Baharin, *Cerne*, 2019, **25**, 18–24.
39 D. Morantes, E. Muñoz, D. Kam and O. Shoseyov, *Nanomaterials*, 2019, **9**(2), 272.
40 C. Lin, T. Zeng, Q. Wang, L. Huang, Y. Ni, F. Huang, X. Ma and S. Cao, *BioResources*, 2018, **13**, 5965–5975.
41 H. S. Hafid, F. N. Omar, E. K. Bahrin and M. Wakisaka, *Bioresour. Bioprocess*, 2023, **10**, 7.
42 D. C. Grahame, *Chem. Rev.*, 1947, **41**, 441–501.
43 L. Bocquet and E. Charlaix, *Chem. Soc. Rev.*, 2010, **39**, 1073–1095.
44 S. Mafé, J. A. Manzanares and P. Ramirez, *Phys. Chem. Chem. Phys.*, 2003, **5**, 376–383.
45 T. Y. George, I. C. Thomas, N. O. Haya, J. P. Deneen, C. Wang and M. J. Aziz, *Appl. Mater. Interfaces*, 2023, **15**, 57252–57264.
46 D. Rahmadiawan, H. Abral, M. A. Azka, S. M. Sapuan, R. I. Admi, S. C. Shi, R. Zainul, N. Azril, A. Zikri and M. Mahardika, *RSC Adv.*, 2024, **14**, 29624–29635.
47 T. Li, S. X. Li, W. Kong, C. Chen, E. Hitz, C. Jia, J. Dai, X. Zhang, R. Briber, Z. Siwy, M. Reed and L. Hu, *Sci. Adv.*, 2019, **5**, eaau4238.
48 R. Yang, S. Liu, L. Zhou, X. Lin and B. Su, *ChemElectroChem.*, 2021, **8**, 585–591.
49 Y. Hu, M. Chen, C. Qin, J. Zhang and A. Lu, *Carbohydr. Polym.*, 2022, **292**, 119650.
50 K. Uetani and K. Hatori, *Sci. Technol. Adv. Mater.*, 2017, **18**, 877–892.
51 M. Antlauf, N. Boulanger, L. Berglund, K. Oksman and O. Andersson, *Biomacromolecules*, 2021, **22**, 3800–3809.
52 S. Shin, S. Bang, J. Choi, H. J. Son, H. Yoon, H. Yun, J. H. Choi and D. Wee, *Int. J. Energy Res.*, 2015, **39**, 851–859.
53 T. T. Wallace, Z. H. Jin, J. Su and J. Electron, *Mater*, 2016, **45**, 2142–2149.
54 H. S. Kim, W. Liu and Z. Ren, *Energy Environ. Sci.*, 2017, **10**, 69–85.
55 S. Mardi, D. Zhao, N. Kim, I. Petsagkourakis, K. Tybrandt, A. Reale and X. Crispin, *Adv. Electron. Mater.*, 2021, **7**, 2100506.
56 X. Zhao, W. Han, C. Zhao, S. Wang, F. Kong, X. Ji, Z. Li and X. Shen, *ACS Appl. Mater. Interfaces*, 2019, **11**, 10301–10309.
57 H. Li, Y. Zong, Q. Ding, W. Han and X. Li, *J. Power Sources*, 2021, **500**, 229992.
58 D. Zhao, A. Würger and X. Crispin, *J. Energy Chem.*, 2021, **61**, 88–103.
59 P. Desmond, K. T. Huisman, H. Sanawar, N. M. Farhat, J. Traber, E. O. Fridjonsson, M. L. Johns, H. C. Flemming, C. Picioreanu and J. S. Vrouwenvelder, *Water Res.*, 2022, **210**, 118031.
60 M. G. Davidson and W. M. Deen, *Macromolecules*, 1988, **21**, 3474–3481.
61 N. Oe, N. Hosono and T. Uemura, *Chem. Sci.*, 2021, **12**, 12576–12586.

